JACS
JOURNAL OF THE AMERICAN CHEMICAL SOCIETY
Article
pubs.acs.org/JACS

Antiferromagnetic Iron Nanocolloids: A New Generation in Vivo T_1 MRI Contrast Agent

Yung-Kang Peng,[†,⊥] Chien-Liang Liu,[†,⊥] Hsieh-Chih Chen,[†] Shang-Wei Chou,[†] Wei-Hsuan Tseng,[†] Yu-Jui Tseng,[†] Chia-Cheng Kang,[‡] Jong-Kai Hsiao,*[,§,∥] and Pi-Tai Chou*[,†]

[†]Department of Chemistry, National Taiwan University, Taipei, Taiwan
[‡]Department of Chemistry, Fu Jen Catholic University, New Taipei City, Taiwan
[§]Department of Medical Imaging, Taipei TzuChi Hospital, The Buddhist Tzuchi Medical foundation, Taipei, Taiwan
[∥]School of Medicine, Tzu-Chi University, Hualien, Taiwan

Supporting Information

ABSTRACT: A novel T_1 agent, antiferromagnetic α-iron oxide-hydroxide (α-FeOOH) nanocolloids with a diameter of 2−3 nm, has been successfully prepared. These nanocolloids, together with a post synthetic strategy performed in mesoporous silica, are a great improvement over the low T_1-weighted contrast common in traditional magnetic silica nanocomposites. The intrinsic antiferromagnetic goethite (α-FeOOH) shows very low magnetization (M_z) of 0.05 emu g^{-1} at H = 2 T at 300 K (0.0006 emu g^{-1} for FeOOH/WMSN-PEG), which is 2 orders of magnitude smaller than any current ultrasmall iron oxide NPs (>5 emu g^{-1}) reported to date, hence ensuring the low r_2 ($\propto M_z$) (7.64 mM^{-1} s^{-1}) and r_2/r_1 ratio (2.03) at 4.7 T. These biodegradable α-FeOOH nanocolloids also demonstrate excellent in vitro cellular imaging and in vivo MR vascular and urinary trace imaging capability with outstanding biocompatibility, which is exceptionally well secreted by the kidney and not the liver as with most nanoparticles, opening up a new avenue for designing powerful antiferromagnetic iron T_1 contrast agents.

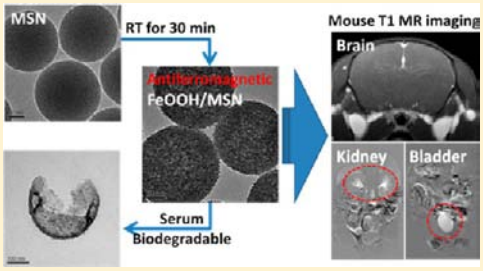

INTRODUCTION

Magnetic colloidal T_1 MRI contrast agents (CAs) (e.g., Gd_2O_3, MnO) have been shown to have potential in biomedical applications.[1,2] These CAs have higher water proton relaxivities than metal-based complexes because metal ions in the nanoparticles (NPs) are densely populated and the techniques of surfactant modification are versatile and well developed, which enable them to attain better functionality and biocompatibility. Unfortunately, both Gd-based (e.g., Gd-complexes,[3−5] Gd_2O_3 NPs[6]) and Mn-based (e.g., MnO,[7,8] Mn_3O_4 NPs[9]) T_1 CAs are hazardous if they dissociate and accumulate in the body, limiting their clinical applications. For instance, an important problem with intravascular Gd-based contrast agents is that transmetalation would result in free Gd(III), and its retention in the human body would potentially cause fatal fibrotic disorder, i.e., nephrogenic systemic fibrosis (NSF).

Alternatively, ultrasmall iron oxide nanoparticles[10−15] (USIONPs) with suppressed magnetization ($M_z^2 \propto r_2$)[16] have recently proved to be a potential T_1 candidate (low r_2/r_1 ratio) due to their superior biocompatibility to manganese oxide NPs and Gd^{3+}-based complex/NPs. Iron ions exist ubiquitously in the living system and serve as a key physiological element for hemoglobin, so their metabolism should be feasible. Recent advances show that USIONPs delivered into the bloodstream eventually become the source of the body iron pool that resides in the liver. To date, preparation of USIONPs can be mainly categorized into hydrophobic and hydrophilic methods. The hydrophobic synthesis[10−12] mainly depends on high-temperature decomposition (>200 °C) of iron precursor (e.g., $Fe(CO)_5$[10] and $Fe(oleate)_3$[11,12]) to obtain homogeneous USIONPs with good quality, which are then transferred to aqueous phase for bioapplication. However, the phase transfer procedure is time-consuming, and sophisticated ligand design is required to provide NPs with properties such as specific targeting, optical imaging, biocompatibility, and drug delivery. In comparison, hydrophilic USIONPs[13−15] can be prepared directly by using tri(ethylene glycol) (or di(ethylene glycol)) as both reductant and surfactant at 200 °C. Unfortunately, such USIONPs have less particle uniformity and thus are inferior in MR relaxivity, since that value is strongly related to size.[12] Moreover, because they are extremely small, in theory, strongly coordinating surfactants should be applied for USIONPs to prevent clustering under physiological conditions, which would result in intensive T_2 contrast increase and hence disappearance of T_1.[11] The strong coordination accordingly minimizes the number of coordinated water molecules (q) to a paramagnetic center, hence the reduction of inner-sphere relaxivity (r_1^{IS}) and overall longitudinal relaxivity (r_1) (see Supporting Information for details).[3] The good dispersity also leads to difficulty in both purification and scaled-up production.

Received: September 13, 2013
Published: November 20, 2013

dx.doi.org/10.1021/ja409490q | J. Am. Chem. Soc. 2013, 135, 18621−18628

From the above points of view, it is urgent to develop biocompatible T_1 CAs with not only superior contrast but also feasibility to be multifunctionalized and scaled-up without trivial processes. We report herein the use of K_2FeO_4 as the iron precursor and the synthesis of magnetic FeOOH nanoparticles with an antiferromagnetic property. To the best of our knowledge, this is the first study exploring the potential of iron-based antiferromagnetic nanoparticles (i.e., FeOOH) in T_1-weighted CAs, for which the surface Fe^{3+} ions contribute to r_1 as the current USIONP does. The as-synthesized antiferromagnetic FeOOH nanoparticles prove to be a superior T_1 CA (cf. USIONPs) due mainly to their extremely low magnetization value (low r_2 and thus low r_2/r_1 ratio is ensured) (vide infra). We also exploit a postsynthesis strategy so that FeOOH NPs can be homogeneously dispersed in the worm-like mesoporous silica (WMSN) framework. Such a structural design not only makes FeOOH NPs inside the WMSN framework free from surfactant coordination (increase parameter q of r_1^{IS}) but also provides mechanical resistance against clustering under physiological conditions. The resulting FeOOH/WMSN-PEG nanocomposites prove to be biodegradable and superior in both in vitro and in vivo T_1 contrast. More importantly, the synthetic process of FeOOH NP is extremely facile, time-saving, eco-friendly, cost-effective, and easy to scale up, making it a promising candidate for biomedical applications.

EXPERIMENTAL SECTION

Synthesis of FeOOH Nanoclusters and Nanoparticles. FeOOH nanoclusters were synthesized by redox reaction between K_2FeO_4 (5 mM) and water molecules at 60 °C. After 10 min of stirring, the samples were centrifuged several times to remove the unreacted chemicals. One milligram of as-prepared nanoclusters were submerged into citric acid solution (1 mM) and sonicated for 120 min. After 8 h of dialysis, the final product, FeOOH NPs, was successfully prepared.

Synthesis of Worm-Like Mesoporous Silica Nanoparticles (WMSNs). To synthesize WMSNs with 200 nm in diameter, 240 mg of CTAB, 2.3 g NH_4OH (30%), 10 mL of ethyl acetate, and 0.25 mL of tetraethyl orthosilicate (TEOS) were added to a mixture of 150 mL of water. The mixture was heated to 60 °C under stirring for 6 h. For the synthesis of 50 nm WMSNs, NH_4F was used as a catalyst for accelerating the hydrolyzation and condensation of silicon sources instead of NH_4OH. Briefly, 364 mg of CTAB, 148 mg of NH_4F, and 0.83 mL of TEOS were added to a mixture of 100 mL of water. The mixture was heated to 80 °C under stirring for 1 h. The resulting WMSNs were then retrieved by repeating the procedures of centrifugation and dispersion in ethanol several times.

Synthesis of FeOOH/WMSN-PEG Nanocomposites. Chemical oxidation−reduction reaction was activated by the treatment of as-prepared WMSNs in K_2FeO_4 aqueous solution. Briefly, 50 mg of as-prepared WMSNs were dispersed into 10 mL of deionized water, and then 10 mL of 1 mM K_2FeO_4 aqueous solution was added into WMSNs dispersions dropwise under magnetic stirring. The mixture was reacted under room temperature and continued for another 30 min. The product was collected by centrifugation and washed with plenty of water under ultrasonic treatment to remove unreacted FeO_4^{2-} ions. The surface modification of PEG proceeded as follows: 30 μL of 2-[methoxy-(polyethyleneoxy)propyl]trimethoxysilane (PEG500-silane, M_w = 460−590, tech-90, Gelest) was added to a mixture of ethanol (30 mL), DI water (6 mL), NH_4OH (28−30 wt %, Fluka) (300 μL), and the as-prepared FeOOH/WMSN (20 mg). After 24 h of stirring, the samples were centrifuged several times to remove the unreacted chemicals. Finally, the surfactant (CTAB) was removed via the ion exchange method, in which the products were transferred to 50 mL of ethanol containing 0.3 g of NH_4NO_3, and the solution was maintained at 60 °C for 2 h. The extraction step was repeated twice to ensure the removal of the surfactants.

Characterizations. The shapes and size distributions of the nanocrystals were measured with a JEOL JEM 1230 transmission electron microscope (TEM). High resolution (HRTEM) images were taken with a JEOL JEM 2100F microscope operated at 200 kV. Experiments of X-ray energy dispersive spectroscopy (EDS) were performed by using a GENESIS 2000 EDS detector connected to the HRTEM instrument. The conventional Formvar coated 200 mesh Cu grids were used for the above-mentioned electron microscope (EM) experiments. Powder X-ray diffraction data was collected on a Bruker D8 Advance diffractometer. The workup procedure was carried out with Cu Kr radiation (λ) 1.54178 Å. Magnetic measurements were performed by superconducting quantum interference device (SQUID) magnetometer (MPMS, Quantum Design). The measurements were recorded between −20000 and 20000 Oe at 300 K. The specific surface area of the sample was calculated based on the Brunauer−Emmett−Teller (BET) equation at P/P_0 between 0.05 and 0.3. The total pore volume was the adsorbed amount at a P/P_0 of 0.99. The pore diameter was calculated from the branch of the adsorption isotherm using a Barrett−Joyner−Halenda (BJH) method. X-ray photoelectron spectrometry (XPS/ESCA) was used to determine the chemical state of Fe. The spectra were recorded with a PHI 5000 VersaProbe scanning ESCA microprobe (ULVAC-PHI, Japan) using a microfocused, monochromatic Al Kα X-ray (25 W, 100 μm). Thermogravimetric analysis (TGA) of the particles was carried out by Dynamic Q500 instrument.

Biodegradation. To evaluate small molecule chelation and degradation of FeOOH/WMSN-PEG, 2 mg of FeOOH/WMSN-PEG was added to a 1.5 mL microcentrifuge tube containing 1 mL of EDTA aqueous solutions (0.1 M). The samples were then placed in a 60 °C water bath and sonicated for 180 min. For degradation of FeOOH/WMSN-PEG in mammalian serum, 2 mg of FeOOH/WMSN-PEG was incubated in 1 mL of FBS at 37 °C for 3 days. TEM images of samples were taken at different time points to monitor the degradation.

In Vitro Cytotoxicity. The cell viability was analyzed by using a colorimetric assay agent, 3-(4,5-dimethylthiazol-2-yl)-2,5-diphenyltetrazolium bromide (MTT, Roche), as described (Mosmann 1983). The HeLa cells were seeded in a 96-well plate with 5×10^4 cells per well in a 90% minimum essential medium (MEM; Cellgro Herndon, VA, USA) supplemented with 10% heat-inactivated fetal bovine serum, penicillin (50 U/mL), and streptomycin (0.05 mg/mL). To contrast with the control, five different dosages of FeOOH/WMSN-PEG were added to each well: 20, 50, 100, 150, and 200 μg/mL. After 12 h of incubation, wells were washed twice with PBS and then incubated with 200 μL of the culture medium with 10% MTT (3-(4,5-dimethylthiazol-2-yl)-2,5-diphenyltetrazolium bromide) agent per well. After 4 h of reaction time, the culture medium was removed and replenished with 200 μL of dimethyl-sulfoxide (Sigma-Aldrich) per well to dissolve the purple MTT formazan crystal. The optical density of these samples was measured at 595 nm. All measurements were done with three replicates using an ELISA reader (VersaMax Microplate Spectrophotometers; Molecular-Devices).

Cell Labeling. Cells (5×10^4 cells per well in 6-well Falcon tissue culture plate) cultured in a 90% minimum essential medium (MEM; Cellgro Herndon, VA, USA) containing 10% fetal bovine serum, penicillin (50 U/mL), and streptomycin (0.05 mg/mL) were incubated for 12 h with 150 μg/mL of FeOOH/WMSN-PEG. After incubation, the culture medium was removed, and the adherent cells were washed twice with PBS. For Prussian blue staining, an as prepared mixed solution of equal parts of 2 N hydrochloric acid and 2% potassium ferrocyanide solution was added 200 μL per well. After 30 min, the supernatant was discarded, and cells were washed with distilled water for several times. The cell samples were observed with an optical microscope (OLYMPUS IX81).

Relaxivity Measurement. The r_1 and r_2 relaxation times were measured at 40 °C using a 0.47 T Minispec spectrometer (Bruker Minispec mq series relaxometer); r_2 relaxation times were determined using a Carr Purcell Meiboom Gill (CPMG) sequence, with a recycle time of 10 s, eight averages with phase cycling, and 180° pulse separation of 1 ms. Monoexponential fitting was performed to even

dx.doi.org/10.1021/ja409490q | J. Am. Chem. Soc. 2013, 135, 18621−18628

echoes over a 250 ms acquisition window. The r_1 relaxation was estimated using inversion recovery techniques, with a recycle time of 10 s, four averages with phase cycling, and eight inversion times logarithmically spaced over the interval 0−2000 ms. Linear regression between r_1 and r_2 and manganese concentration was performed using standard techniques.

In Vitro MR Imaging. MRI was performed using a clinical 3 T MR system (Signa Excite, GE Healthcare, USA). The cell samples were centrifuged in test tubes bathing in a homemade water tank. The tank was then placed in an 8 channel head coil. Two dimension T_1-weighted fast spin echo pulse sequences were used (TR/TE = 550/13 ms). The slice thickness was 1.0 mm with a 0.5 mm gap, and the field of view (FOV) was 14 cm × 10 cm. The matrix size was 288 × 192. Total scan time was 4 min and 5 s at the NEX of 2. The images were then analyzed at a workstation provided by GE Healthcare (Advantage workstation 4.2).

In Vivo Experiment. All animals were initially anesthetized with 5% isoflurane at 1 L min^{-1} air flow. When fully anesthetized, the animal was placed in a prone position and fitted with a custom-designed head holder inside the magnet. Isoflurane was then maintained with 1−1.5% and 0.8−1.2% for rat and mouse, respectively, at 1 L min^{-1} air flow throughout the experiments. Sprague−Dawley rat brain experiments were performed in a Biospec 4.7 T spectrometer before and at different times after the injection of FeOOH/WMSN-PEG with (T1/T2) TR = 500/5000 ms, (T1/T2) TEeff = 8/70 ms, FOV = 7 cm × 7 cm, slice thickness = 1.3 mm, and matrix size = 256 × 128 (zero-padded to 256 × 256) with six repetitions. Typically, nanoparticles suspended in PBS buffer (0.1 mL) were administrated to Institute of Cancer Research mice (8 weeks of age, body mass ∼300 g) via femoral vein injection at a dose of 1 mg Fe kg^{-1} (body weight). Mice body experiments were performed in a Pharmascan 7 T spectrometer before and at different times after the injection of FeOOH/WMSN-PEG with TR = 550 ms, TE = 10.5 ms, FOV = 3.5 cm × 3.5 cm, slice thickness = 1.2 mm, and matrix size = 256 × 128 (zero-padded to 256 × 256) with eight repetitions. Typically, nanoparticles suspended in PBS buffer (0.1 mL) were administrated to Institute of Cancer Research mice (8−10 weeks of age, body mass ∼25 g) via femoral vein injection at a dose of 1 mg Fe kg^{-1} (body weight). The percentage of signal-to-noise (SNR) change for preinjection versus postinjection T_2WI and T_2WI were calculated according to the following formula: % SNR difference = 100 × $((SNR)_{post} - (SNR)_{pre})/(SNR)_{pre}$.

RESULTS AND DISCUSSION

Preparation of Iron Oxide-Hydroxide (FeOOH). More than one and a half centuries since the synthesis of ferrate (FeO_4^{-2}), its chemistry remains relatively unknown because of its unclear reactivity.[17] K_2FeO_4 has been employed in wastewater treatment as a strong oxidant for organic contaminants and as a biocide due to its unique property of "green chemistry". It decomposes in contact with water, yielding the red-brown precipitate iron(III) oxide-hydroxide, which is nontoxic and environment-friendly. The reaction stoichiometry can be expressed as:

$$4K_2FeO_4 + 10H_2O \rightarrow 4FeO(OH)\cdot H_2O\downarrow + 3O_2\uparrow + 8KOH \quad (1)$$

Recently, a seminal study by Licht et al.[18] demonstrated that alkaline ferrate/Zn batteries had 50% greater capacity than conventional alkaline batteries. Ever since then, the studies of ferrate[19,20] used as a cathode have been attracting much attention because ferrate is capable of performing three-electron reduction. Amid the research of ferrate, in serendipity, we discovered that the main product of eq 1, iron oxide-hydroxide (FeOOH), could be a better substitute T_1 material for current USIONPs (ferrimagnetic) as a result of its antiferromagnetic property, which intrinsically ensures low r_2. Moreover, eq 1 is a first-order spontaneous reaction ($\Delta G < 0$), so the reaction takes place effectively at room temperature (RT), and no other valence states of iron (i.e., 2+, 4+ and 5+) are generated except Fe^{3+}.

Scheme 1 schematically depicts the synthesis of FeOOH NPs. First, the FeOOH clusters were directly prepared by redox reaction between K_2FeO_4 and water molecules. The as-prepared clusters were submerged into citric acid (aqueous solution) under sonication, and then the final products, FeOOH NPs, were successfully prepared. As shown in Figure 1a, FeOOH nanoclusters of about 40 nm in diameter are generated by redox reaction between K_2FeO_4 (5 mM) and water molecules at 60 °C for as short as 10 min. The clusters, consisting of several crystalline FeOOH particles (∼ 6 nm) (Figure 1a inset), are then disassembled into monodispersed FeOOH NPs (Figure 1b) by surfactant (citric acid) adsorption under sonication for 120 min. This disassembly process can be clearly seen in Supplementary Figure S1. Supplementary Table S1 shows the corresponding relaxivities of the FeOOH nanocluster and the FeOOH NP. Accordingly, the longitudinal relaxation of the FeOOH NP is higher (2.12 mM^{-1} s^{-1}) than that of its cluster form (0.48 mM^{-1} s^{-1}), mainly due to the increased surface Fe^{3+} concentration (about 50 times). Even though it is facile to prepare antiferromagnetic FeOOH NP, at this stage, it is not competitive with current ferrimagnetic USIONP (<4 nm) because of the inhomogeneity and relatively low surface-to-volume ratio, both of which are critical for longitudinal relaxivity.

Scheme 1. Schematic Representation the Synthesis of FeOOH NPs[a]

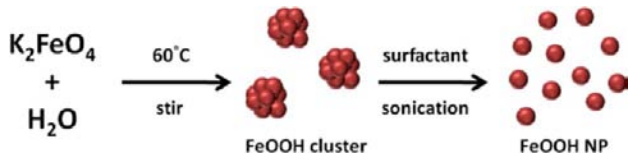

[a]FeOOH clusters were directly prepared by redox reaction between K_2FeO_4 (5 mM) and water molecules at 60°C for 10 min. The as-prepared clusters were submerged into citric $acid_{(aq)}$ under sonication for 120 min, and then the final product, FeOOH NPs, were successfully prepared (see Experimental Section for detail).

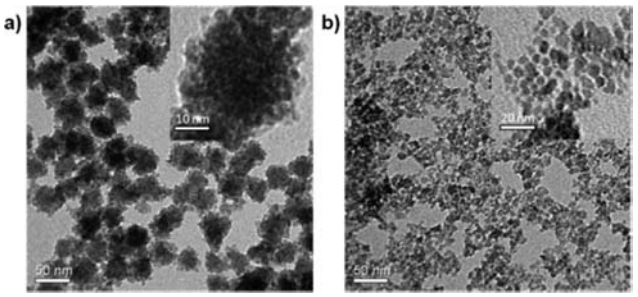

Figure 1. TEM images of the FeOOH (a) clusters and (b) NPs.

WMSN Templating. For further improvement, WMSN is chosen as an ideal template. In addition to its well-developed sol−gel chemistry for versatile applications,[21−26] more importantly, the average pore size of WMSN is ∼2.5 nm, which matches well the diameter of the nanocolloids to be

dx.doi.org/10.1021/ja409490q | J. Am. Chem. Soc. 2013, 135, 18621−18628

synthesized inside in an aim to avoid clustering as well as to greatly enhance the overall surface area of FeOOH NPs.

Scheme 2 shows the overall schematic illustration of the synthetic procedure of FeOOH/WMSN NPs. Upon introduction of WMSN into $K_2FeO_{4(aq)}$, under a mild reaction environment (e.g., 1 mM K_2FeO_4 at RT), it was expected that the FeOOH particles would be well dispersed in WMSN (denoted as FeOOH/WMSN*, where * indicates using CTAB washed WMSN as a template) and that they would be easily separable from any WMSN-free, small FeOOH particles in the stock solution via centrifugation. Interestingly, after centrifugation, as evidenced by the TEM image (Supplementary Figure S2b), no free FeOOH particles were observed outside the FeOOH/WMSN* nanocomposite (NC). Though it is difficult to identify inner FeOOH particles from the TEM images of FeOOH/WMSN* (Supplementary Figure S2c, cf. TEM image of WMSN* (Supplementary Figure S2a)), the existence of iron was clearly verified (~0.64% by atom) using energy-dispersive X-ray (EDX) spectroscopy (Supplementary Figure S2d).

Scheme 2. Schematic representation of the synthesis of FeOOH/WMSN nanocomposites (NCs)[a]

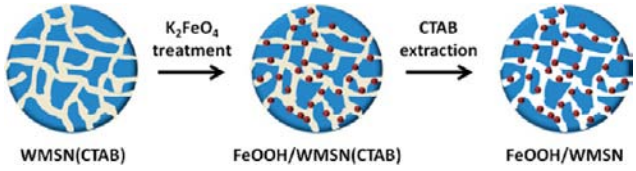

[a]WMSN(CTAB) was prepared in an alkaline ethanol–water solution using CTAB surfactant as the template. Second, FeOOH in the nanochannels was prepared by dispersing WMSN(CTAB) into $K_2FeO_{4(aq)}$. The CTAB species were subsequently washed by NH_4NO_3 solution, and the resulting FeOOH/WMSN NCs were successfully prepared.

However, with CTAB-stuffed mesoporous WMSN (Figure 2a) used as a template, the number of FeOOH particles generated in WMSN increased significantly, as clearly confirmed by TEM imaging of FeOOH/WMSN (Figure 2b, see Supplementary Figure S3a for low magnification image; hereafter, WMSN denotes the CTAB-filled WMSN). Moreover, the EDX data of FeOOH/WMSN (Supplementary Figure S3b) showed ~12% iron content, which is about 20-fold higher than that of FeOOH/WMSN*. The corresponding longitudinal (r_1) and transverse (r_2) relaxivity of FeOOH/WMSN* and FeOOH/WMSN at 0.47 T are listed in Supplementary Table S1. Both had r_2/r_1 ratios of ~1.9, which to the best of our knowledge is the lowest ever reported for iron-based colloidal T_1 contrast agents.[10−15] Also noted is that FeOOH/WMSN had a higher r_1 value of 4.03 mM^{-1} s^{-1} (cf. 2.74 mM^{-1} s^{-1} for FeOOH/WMSN*). The results indicate that FeOOH/WMSN releases longitudinal relaxation more efficiently than FeOOH/WMSN* does. Taking the silica NPs as the vehicle for FeOOH, the FeOOH/WMSN delivers up to 20 times more FeOOH particles than FeOOH/WMSN* does. The role of the CTAB molecule during the K_2FeO_4 treatment is important. Though CTAB has been demonstrated to be a reducing agent,[27] we tend to believe that CTAB may not only act as the surfactant but also locally reduce the redox barrier of the reaction (see eq 1) in the pores by forming a meta-thermodynamically stable species during the K_2FeO_4 treatment, enhancing the production of FeOOH NPs. The final nanocomposite, FeOOH/WMSN, possessed an r_1 value as high as 4.03; consequently, the r_2/r_1 ratio was measured to be as low as 1.97.

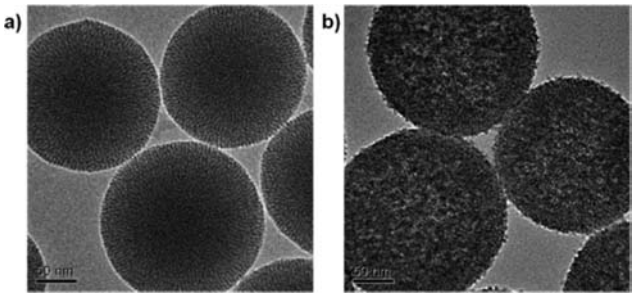

Figure 2. TEM images of (a) WMSN(CTAB) and (b) FeOOH/WMSN.

Characterization of FeOOH/WMSN-PEG. Relevant structure and property characterizations are elaborated in the Supporting Information (see Figure S4 for details). The XPS (Supplementary Figure S4d) result showed no detectable high iron valence states (>3). Since the iron ions were determined to be solely Fe^{3+}, further reduction for achieving a high S value (i.e., a large number of unpaired S-state (not L-state) electrons and hence an increase of r_1 relaxivity was unnecessary. Moreover, the XRD patterns of FeOOH clusters (Supplementary Figure S5) matched very well the characteristic peaks of α-phase iron oxide-hydroxide (α-FeOOH). We therefore anticipated that the as-prepared FeOOH particles, which were homogeneously dispersed in the WMSN, were α-phase in nature. Further support of this viewpoint is given by the HRTEM measurement of the as-prepared FeOOH particles (Supplementary Figure S6). The lattice spacing is calculated to be 0.248 nm, which originates from the (111) plane of α-FeOOH structure. It is noteworthy that the extremely small magnetization of FeOOH/WMSN (0.0006 emu g^{-1}) at H = 2 T, 300 K (Supplementary Figure S4f) was nearly 4 orders of magnitude less than that of the typical T_1-weighted ultrasmall Fe_3O_4 NPs (>5 emu g^{-1}).[10−15] To the best of our knowledge, this is the first report to demonstrate that FeOOH NPs, for which surface Fe^{3+} ions contribute to r_1 as the Fe_3O_4 particle does, can be a superior T_1 CA agent (cf. Fe_3O_4 particles) due mainly to its extremely low magnetization value (low r_2). To strengthen the biocompatibility, we then prepared FeOOH/WMSN encapsulated by poly(ethylene glycol) (PEG), forming a FeOOH/WMSN-PEG nanocomposite, which is particularly suitable for long circulating in vivo imaging systems to bypass the reticuloendothelial system (RES).[1] The successful PEG modification and following CTAB extraction were verified by thermal gravimetric analysis (TGA), shown in Supplementary Figure S7. The T_1-weighted MR imaging capability of the FeOOH/WMSN-PEG nanocomposite was evaluated, showing that the MR signal intensity increased apparently as the concentration of Fe ions increased (see Supplementary Figure S8).

Degradation of FeOOH/WMSN-PEG in Mammalian Serum. Very recently, the incorporation of iron(III) into the silica matrix has been shown to promote the degradation of silica matrix in human serum and fetal bovine serum due to the presence of iron-chelating agents.[28] We thus anticipate a similar benign metabolism process for the FeOOH/WMSN-PEG T_1 CA presented here. Small molecular chelation was initially used to determine whether silica degradation could be promoted by iron removal. In this aspect, EDTA, which strongly binds

iron(III) with a formation constant of $\sim 10^{25}$, was used to evaluate whether silica degradation could be promoted by iron removal. The samples were then placed in a 60 °C water bath and sonicated for 180 min, giving no apparent morphology change for WMSN-PEG (Supplementary Figure S9a); however, collapse of the silica structure was clearly observed once FeOOH NPs were introduced. The degradation of the FeOOH/WMSN-PEG nanocomposites began with shrinkage of the interior silica (first 90 min, see Supplementary Figure S9d) rather than collapse of the outmost surface (after 90 min, Supplementary Figure S9g), possibly due to the PEG modification, resulting in different degrees of condensation.[29] The morphology evolution of FeOOH/WMSN-PEG on exposure to EDTA (aqueous solution) under sonication is summarized in Supplementary Figure S10. To determine whether the biological ligands for iron(III) present in mammalian serum, i.e., transferrin, an iron(III) chelating protein with a formation constant of $\sim 10^{20}$, could also affect a similar degradation process relevant to in vivo dosing, the biodegradability of FeOOH/WMSN-PEG was then tested by immersion in fetal bovine serum (FBS) at 37 °C (physiological temperature) with shaking for various time periods. The results showed that WMSN-PEG remained intact in FBS for up to 3 days (Figure 3b); in stark contrast; FeOOH/WMSN-PEG became hollow within 24 h (Figure 3c) and eventually collapsed (Figure 3d).

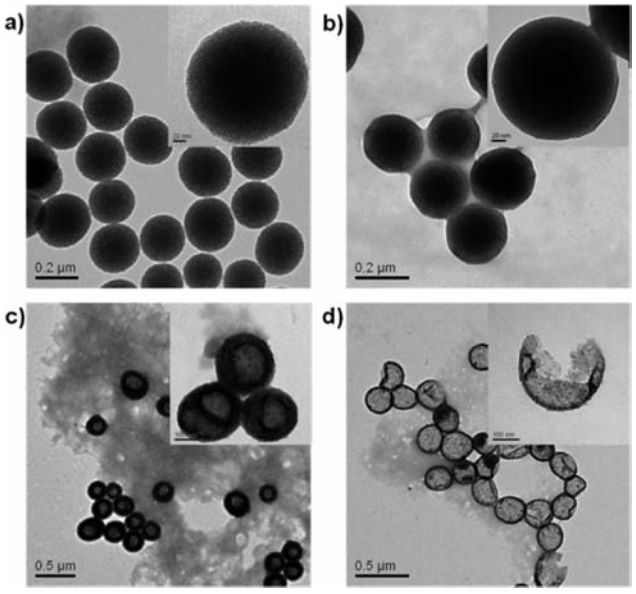

Figure 3. TEM images of (a,b) WMSN-PEG and (c,d) FeOOH/WMSN-PEG exposed to fetal bovine serum (FBS) at 37 °C for (a,c) 24 h and (b,d) 3 days.

We therefore conclude that the degradation of FeOOH/WMSN-PEG is greatly accelerated relative to that of WMSN-PEG under the presence of iron chelating agents, manifesting its potential biodegradability. As for the decomposed WMSN, it has been reported that nearly 95% of the degradation products of mesoporous silica nanoparticles could be safely excreted through urine and feces 4 days after tail vein injection.[30]

In Vitro Cellular Testing and in Vivo MR Imaging. To prevent aggressive ingestion by the reticuloendotherial system (RES) in the liver and to compete with USIONPs, the hydrodynamic size of the particle needs to be <100 nm to prolong the in vivo circulation time.[31] Therefore, the average size of the FeOOH/WMSN-PEG was reduced to 47.1 ± 3.1 nm in diameter for this application (Supplementary Figure S11b). The dynamic light scattering (DLS) data revealed a larger hydrodynamic diameter, about 70.4 nm in PBS solution, due to the hydration layer of PEG. We verified the biocompatibility of this new T_1 CA by determining the cytotoxicity of the HeLa cell line, the first human cancer cell line.

As shown in Supplementary Figure S12, the viability of HeLa cells was almost 100%, even up to 150 μg/mL after 12 h of incubation, providing clear evidence that the cytotoxicity of the NCs is negligible. The uptake of the FeOOH/WMSN-PEG was confirmed histologically by Prussian blue staining (Figure 4a).

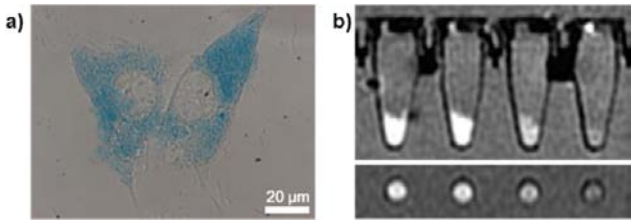

Figure 4. (a) Prussian blue stained images of FeOOH/WMSN-PEG treated HeLa cells. See Supplementary Figure S13 for low magnification image. (b) Side and bottom views of T_1-weighted images of HeLa cells treated with FeOOH/WMSN-PEG at different Fe concentrations. From left to right: [Fe] = 1.21, 0.6, 0.3, 0 (control) mM.

Figure 4b shows the MR images of the collected cell pellets fed with FeOOH/WMSN-PEG at different iron concentrations. The signal intensity increased significantly as iron content increased, which firmly supports the labeling capability of FeOOH/WMSN-PEG and demonstrates its potential application for cell trafficking, which is of biomedical importance in stem cell technology. To fully demonstrate the power of FeOOH/WMSN-PEG in brain and vascular MR imaging, we established an in vivo MR imaging animal model with a 4.7 T MR system. Figure 5c shows enhancement in the superior sagittal sinus and bilateral internal carotid arteries, the most important vascular structure of the rat brain. The signal-to-noise ratio (SNR) of the sagittal sinus before and after administration rose up to 281%, but the SNR in cortex remained nearly unchanged. This makes FeOOH/WMSN-PEG a superior vascular diagnosis agent for disease diagnosis, such as arterial occlusion commonly seen in stroke and coronary heart disease patients and venous thrombosis in patients with coagulopathy. When FeOOH/WMSN-PEG (1 mg of Fe measured by ICP-AES per kilogram of mouse body weight) was intravenously administrated to a mouse, a time course of signal enhancement was clearly observed in T_1-weighted imaging of the kidney (Figure S14 and Figure S15), but there was no apparent signal enhancement in T_1- or T_2-weighted imaging of the liver (Figure S16 and Figure S17). The SNR of the renal pelvis rose 224% after FeOOH/WMSN-PEG administration, followed by a decrease to 145% 40 min after injection and returning to the precontrast image 1.5 h after injection (Supplementary Figure S15a). We observed sufficient FeOOH/WMSN-PEG excretion by monitoring changes in signal intensity in the renal cortex, medulla, and pelvis for 2 h, reflecting efficient particle excretion into urine.

dx.doi.org/10.1021/ja409490q | J. Am. Chem. Soc. 2013, 135, 18621−18628

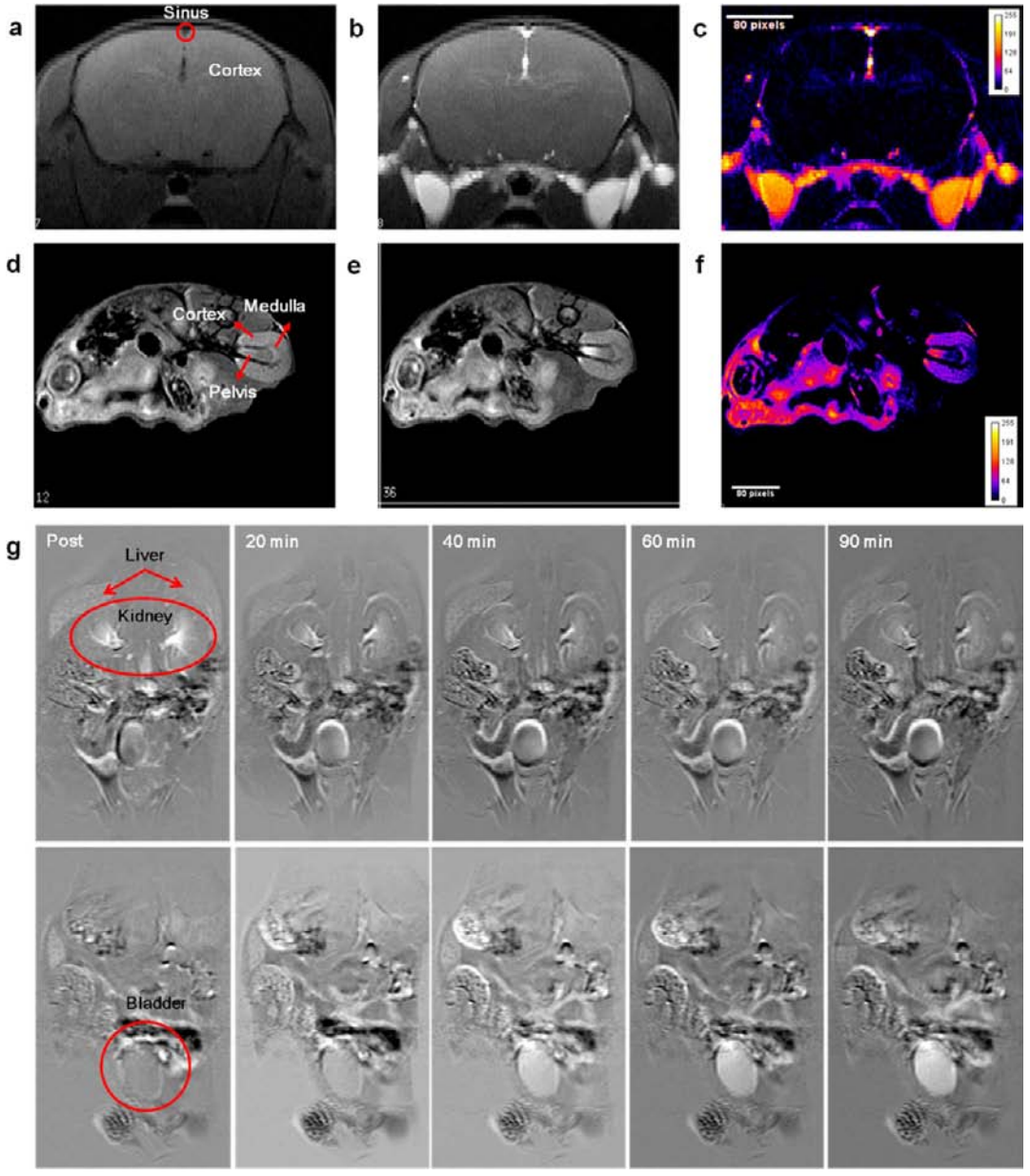

Figure 5. In vivo T_1-weighted image of mouse brain, kidney, and bladder. (a–c) T_1-weighted image of mouse brain at (a) 0 and (b) 10 min, and (c) subtraction image of these two time frames. (d–f) T_1-weighted image of mouse kidney at (d) 0 and (e) 10 min and (f) subtraction image of these two time frames. (g) Subtraction T_1-weighted images of a mouse liver and kidney (first row) and bladder (second row) 10, 20, 40, 60, and 90 min after intravenous injection of FeOOH/WMSN-PEG. Sequential enhancement of renal pelvis followed by urinary bladder is noted.

The above results evidently demonstrate that most FeOOH/WMSN-PEG can escape the surveillance of the reticuloendothelial system (RES) of the liver and can be further secreted by kidneys. Twenty minutes after the injection, the particles accumulated in the bladder, as clearly evidenced by a striking positive contrast, appears first in the mouse kidney and then in the bladder (Figure 5g). As shown in Supplementary Figure S18, the mouse urine collected 2 h after tail vein injection was further analyzed by ICP-MS, and the result confirmed that the particles can be efficiently and safely excreted in the urine. Unlike superparamagnetic iron oxide, Ferucarbotran, which can be metabolized by the hepatic pathway and is used to image liver tumors, we propose FeOOH/WMSN-PEG, which are metabolized by the renal pathway, as a potential contrast agent for studying renal anatomy, glomerular filtration, and urinary tract tumor detection, and more importantly, as an alternative T_1 CA (cf. clinical gadolinium complex) for patients with renal failure.

Outlook. It is also worth noting here that no special equipment is necessary for this method, and when the reactors are set up in parallel, gram-scale production of FeOOH/WMSN-PEG can be readily prepared (Supplementary Figure S19). This synthetic process is therefore facile (room temperature for 30 min), cost-effective, and eco-friendly in both precursor (K_2FeO_4 and H_2O) and product (FeOOH). By carefully controlling the reaction kinetics of eq 1, we successfully prepared FeOOH functionalized hollow mesoporous silica spheres (HMSS) from WMSN in one step (Figure 6e) (details of mechanism will be discussed and published elsewhere). Recently, T_1-HMSS has been demonstrated a promising theranostic agent because of its extremely high contrast agent/drug loading capacity.[32,33]

dx.doi.org/10.1021/ja409490q | J. Am. Chem. Soc. 2013, 135, 18621–18628

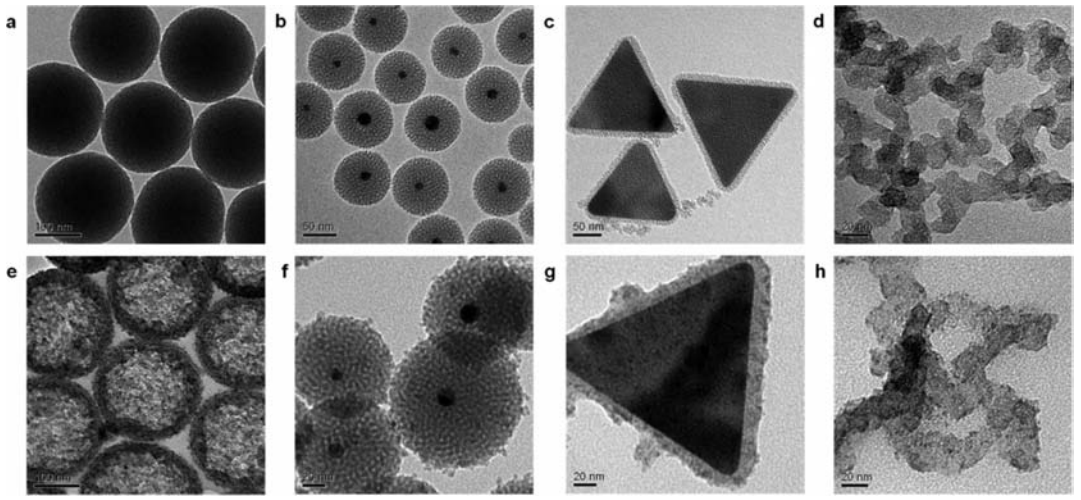

Figure 6. TEM images of (a–d) various templates/substrates (a) WMSN, (b) AuAg@mSiO$_2$, (c) Au prism@mSiO$_2$, and (d) activated carbon. (e–h) Their corresponding FeOOH-functionalized nanocomposites (e), FeOOH-functionalized hollow mesoporous silica spheres (FeOOH-HMSS), (f) AuAg@FeOOH/mSiO$_2$, (g) Au prism@FeOOH/mSiO$_2$, (h) FeOOH/activated carbon. See Supplementary Figure S20 for corresponding energy-dispersive X-ray (EDX) spectroscopy analysis of nanocomposites in panels a–h.

During the progress of this seminal study, based on eq 1, various FeOOH/mesoporous silica coated structures have been successfully fabricated, for example, the AuAg@FeOOH/mSiO$_2$ (Figure 6f) and Au prism@FeOOH/mSiO$_2$ (Figure 6g), by using core@mSiO$_2$ nanocomposites as the substrate/template. Moreover, the core can be any materials in any shape, e.g., alloy (AuAg, Figure 6b), metal (Au prism, Figure 6c and Au rod, Supplementary Figure S21a), semiconductor (hollow SiO$_2$, Supplementary Figure S21b), magnetic (MnO, Supplementary Figure S21c), and up-conversion (Supplementary Figure S21d) nanoparticles, which greatly expand their potential applications in emerging fields such as MRI (T_1-weighted CAs) and catalysis (superoxide-driven Fenton reaction[34] and catalytic ozonation[35]). It is also feasible to transfer FeOOH nanocolloids directly to nonoxide substrate/template such as activated carbon, which is a FDA-approved porous template (Figure 6h), via heterogeneous nucleation, so that no linker molecules are required.

CONCLUSION

In summary, a novel T_1 contrast agent, antiferromagnetic α-FeOOH nanocolloids with a diameter of 2–3 nm, has been successfully prepared in the mesopores of WMSNs. The geometric confinement of WMSN prevents the aggregation of inner surfactant-free particles and hence optimizes their homogeneity. Consequently, both surface Fe^{3+} concentration and coordinated water molecules (q) substantially increase, boosting the r_1 relaxivity. The resulting iron oxide-hydroxide (FeOOH) NPs possess the lowest r_2/r_1 ratio yet reported and reveal magnetization (r_2) that is 2 orders of magnitude lower than that of the current ultrasmall iron oxide (Fe_3O_4) NPs. The resulting FeOOH/WMSN nanocomposites have a 20-fold enhancement in r_1 relaxivity, as large as our previously reported H-MnO@mSiO$_2$.[25,36] FeOOH/WMSN-PEG is also superior in both in vitro and in vivo MRI imaging and has excellent biocompatibility and biodegradability. In the end, we show the prospects for use of this new nanomaterial and the corresponding methodology, which should pave the way for various brilliant results en route to clinical T1MRI contrast agents.

ASSOCIATED CONTENT

Supporting Information

The extension of SBM theory for accessing the performance of particulate FeOOH; relaxation properties of the nanocomposites; additional data regarding the characterizations of nanocomposites, including EDS, XRD, BET, XPS, SQUID, TGA and HRTEM; the TEM images of morphology evolution of FeOOH/WMSN-PEG on exposure to EDTA(aq) under sonication at 60 °C; in vitro cellular MTT Assay and Prussian blue stained image of FeOOH/WMSN-PEG treated HeLa cells; a time course of T_1 and T_2 MR imaging of a mouse liver and kidney after tail vein injection of FeOOH/WMSN-PEG; and EDX spectroscopy analysis of various FeOOH functionalized nanocomposites. This material is available free of charge via the Internet at http://pubs.acs.org.

AUTHOR INFORMATION

Corresponding Authors

jongkai@tzuchi.com.tw
chop@ntu.edu.tw

Author Contributions

$^{\perp}$These authors contributed equally to this work.

Notes

The authors declare no competing financial interest.

ACKNOWLEDGMENTS

This work was supported by the National Science Council, Taiwan (99-2314-B-303-012-MY3; 102-2628-B-303-001-MY3). We thank the Taiwan Mouse Clinic, which is funded by the National Research Program for Biopharmaceuticals (NRPB) at the National Science Council of Taiwan for technical support in mouse experiment. The authors thank Ya-Yun Yang in Instrumentation Center, National Taiwan University, for assistance in the obtainment of HRTEM images.

REFERENCES

(1) Na, H. B.; Sang, I. C.; Hyeon, T. *Adv. Mater.* **2009**, *21*, 2133–2148.
(2) Na, H. B.; Hyeon, T. *J. Mater. Chem.* **2009**, *19*, 6267–6273.

(3) Ananta, J. S.; Godin, B.; Sethi, R.; Moriggi, L.; Liu, X.; Serda, R. E.; Krishnamurthy, R.; Muthupillai, R.; Bolskar, R. D.; Helm, L.; Ferrari, M.; Wilson, L. J.; Decuzzi, P. *Nat. Nanotechnol.* **2010**, *5*, 815−821.
(4) Taylor, K. M. L.; Kim, J. S.; Rieter, W. J.; An, H.; Lin, W.; Lin, W. *J. Am. Chem. Soc.* **2008**, *130*, 2154−2155.
(5) Alric, C.; Taleb, J.; Duc, G. L.; Mandon, C.; Billotey, C.; Meur-Herland, A. L.; Brochard, T.; Vocanson, F.; Janier, M.; Perriat, P.; Roux, S.; Tillement, O. *J. Am. Chem. Soc.* **2008**, *130*, 5908−5915.
(6) Bridot, J.-L.; Faure, A.-C.; Laurent, S.; Rivière, C.; Billotey, C.; Hiba, B.; Janier, M.; Josserand, V.; Coll, J.-L.; Elst, L V.; Muller, R.; Roux, S.; Perriat, P.; Tillement, O. *J. Am. Chem. Soc.* **2007**, *129*, 5076−5084.
(7) Na, H. B.; Lee, J. H.; An, K.; Park, Y. I.; Park, M.; Lee, I. S.; Nam, D.-H.; Kim, S. T.; Kim, S.-H.; Kim, S.-W.; Lim, K.-H.; Kim, K.-S.; Kim, S.-O.; Hyeon, T. *Angew. Chem., Int. Ed.* **2007**, *46*, 5397−5401.
(8) An, K.; Kwon, S. G.; Park, M.; Na, H. B.; Baik, S.-I.; Yu, J. H.; Kim, D.; Son, J. S.; Kim, Y. W.; Song, I. C.; Moon, W. K.; Park, H. M.; Hyeon, T. *Nano Lett.* **2008**, *8*, 4252−4258.
(9) Shin, J.; Anisur, R. M.; Ko, M. K.; Im, H. G.; Lee, J. H.; Lee, I. S. *Angew. Chem., Int. Ed.* **2009**, *48*, 321−324.
(10) Taboada, E.; Rodríguez, E.; Roig, A.; Oró, J.; Roch, A.; Muller, R. N. *Langmuir* **2007**, *23*, 4583−4588.
(11) Tromsdorf, U. I.; Bruns, O. T.; Salmen, S. C.; Beisiegel, U.; Weller, H. *Nano Lett.* **2009**, *9*, 4434−4440.
(12) Kim, B. H.; Lee, N.; Kim, H.; An, K.; Park, Y. I.; Choi, Y.; Shin, K.; Lee, Y.; Kwon, S. G.; Na, H. B.; Park, J.-G.; Ahn, T.-Y.; Kim, Y.-W.; Moon, W. K.; Choi, S. H.; Hyeon, T. *J. Am. Chem. Soc.* **2011**, *133*, 12624−12631.
(13) Hu, F.; MacRenaris, K. W.; Waters, E. A.; Liang, T.; Schultz-Sikma, E. A.; Eckermann, A. L.; Meade, T. J. *J. Phys. Chem. C* **2009**, *113*, 20855−20860.
(14) Hu, F.; Jia, Q.; Li, Y.; Gao, M. *Nanotechnology* **2011**, *22*, 245604.
(15) Shen, L.-H.; Bao, J.-F.; Wang, D.; Wang, Y.-X.; Chen, Z.-W.; Ren, L.; Zhou, X.; Ke, X.-B.; Chen, M.; Yang, A.-Q. *Nanoscale* **2013**, *5*, 2133−2141.
(16) Roch, A.; Gossuin, Y.; Muller, R. N.; Gillis, P. *J. Magn. Magn. Mater.* **2005**, *293*, 532−539.
(17) Goff, H.; Murmann, R. K. *J. Am. Chem. Soc.* **1971**, *93*, 6058−6065.
(18) Licht, S.; Wang, B.; Ghosh, S. *Science* **1999**, *285*, 1039−1042.
(19) Bouzek, K.; Schmidt, M. J.; Wragg, A. A. *Electrochem. Commun.* **1999**, *1*, 370−374.
(20) Licht, S.; Wang, B.; Ghosh, S.; Li, J.; Tel-Vered, R. *Electrochem. Commun.* **2000**, *2*, 535−540.
(21) Liong, M.; Lu, J.; Kovochich, M.; Xia, T.; Ruehm, S. G.; Nel, A. E.; Tamanoi, F.; Zink, J. I. *ACS Nano* **2008**, *2*, 889−896.
(22) Kim, J.; Kim, H. S.; Lee, N.; Kim, T.; Kim, H.; Yu, T.; Song, I. C.; Moon, W. K.; Hyeon, T. *Angew. Chem., Int. Ed.* **2008**, *47*, 8438−8441.
(23) Joo, S. H.; Park, J. Y.; Tsung, C.-K.; Yamada, Y.; Yang, P.; Somorjai, G. A. *Nat. Mater.* **2009**, *8*, 126−131.
(24) Thomas, C. R.; Ferris, D. P.; Lee, J.-H.; Choi, E.; Cho, M. H.; Kim, E. S.; Stoddart, J. F.; Shin, J.-S.; Cheon, J.; Zink, J. I. *J. Am. Chem. Soc.* **2010**, *132*, 10623−10625.
(25) Peng, Y.-K.; Lai, C.-W.; Liu, C.-L.; Chen, H.-C.; Hsiao, Y.-H.; Liu, W.-L.; Tang, K.-C.; Chi, Y.; Hsiao, J.-K.; Lim, K.-E.; Liao, H.-E.; Shyue, J.-J.; Chou, P.-T. *ACS Nano* **2011**, *5*, 4177−4187.
(26) Pan, L.; He, Q.; Liu, J.; Chen, Y.; Ma, M.; Zhang, L.; Shi, J. *J. Am. Chem. Soc.* **2012**, *134*, 5722−5725.
(27) Dong, X.; Shen, W.; Zhu, Y.; Xiong, L.; Shi, J. *Adv. Funct. Mater.* **2005**, *15*, 955−960.
(28) Mitchell, K. K. P.; Liberman, A.; Kummel, A. C.; Trogler, W. C. *J. Am. Chem. Soc.* **2012**, *134*, 13997−14003.
(29) Chen, Y.; Chen, H.; Guo, L.; He, Q.; Chen, F.; Zhou, J.; Feng, J.; Shi, J. *ACS Nano* **2010**, *4*, 529−539.
(30) Lu, J.; Liong, M.; Li, Z.; Zink, J. I.; Tamanoi, F. *Small* **2010**, *6*, 1794−1805.
(31) Lu, F.; Wu, S. H.; Hung, Y.; Mou, C. Y. *Small* **2009**, *5*, 1408−1413.
(32) Chen, Y.; Chen, H.; Sun, Y.; Zheng, Y.; Zeng, D.; Li, F.; Zhang, S.; Wang, X.; Zhang, K.; Ma, M.; He, Q.; Zhang, L.; Shi, J. *Angew. Chem., Int. Ed.* **2011**, *50*, 12505−12509.
(33) Chen, Y.; Yin, Q.; Ji, X.; Zhang, S.; Chen, H.; Zheng, Y.; Sun, Y.; Qu, H.; Wang, Z.; Li, Y.; Wang, X.; Zhang, K.; Zhang, L.; Shi, J. *Biomaterials* **2012**, *33*, 7126−7137.
(34) Zhang, G.; Wang, S.; Yang, F. *J. Phys. Chem. C* **2012**, *116*, 3623−3634.
(35) Zhang, T.; Lin, C.; Ma, J.; Tian, H.; Qiang, Z. *Appl. Catal., B* **2008**, *82*, 131−137.
(36) Peng, Y.-K.; Lai, C.-W.; Hsiao, Y.-H.; Tang, K.-C.; Chou, P.-T. *Mater. Express* **2011**, *1*, 136−143.